Supporting Information

High-performance hierarchical O-SnS/I-$ZnIn_2S_4$ photodetectors by leveraging the synergy of optical regulation and band tailoring

Qiaojue Ye,[ab#] Degao Xu,[c#] Biao Cai,[c#] Jianting Lu,[a] Huaxin Yi,[a] Churong Ma,[d] Zhaoqiang Zheng,[e] Jiandong Yao,*[ab] Gang Ouyang*[c] and Guowei Yang[ab]

[a] State Key Laboratory of Optoelectronic Materials and Technologies, Nanotechnology Research Center, School of Materials Science & Engineering, Sun Yat-sen University, Guangzhou, 510275, Guangdong, P. R. China

[b] Guangzhou Key Laboratory of Flexible Electronic Materials and Wearable Devices, Sun Yat-sen University, Guangzhou, 510275, Guangdong, P. R. China

[c] Key Laboratory of Low-Dimensional Quantum Structures and Quantum Control of Ministry of Education, Key Laboratory for Matter Microstructure and Function of Hunan Province, School of Physics and Electronics, Hunan Normal University, Changsha 410081, China

[d] Guangdong Provincial Key Laboratory of Optical Fiber Sensing and Communications, Institute of Photonics Technology, Jinan University, Guangzhou, 511443, China.

[e] School of Materials and Energy, Guangdong University of Technology, Guangzhou, 510006, Guangdong, P. R. China

[#]These authors contribute equally to this work

*Corresponding authors: yaojd3@mail.sysu.edu.cn, gangouy@hunnu.edu.cn

Keywords: 2D layered materials, photodetectors, $SnS/ZnIn_2S_4$ heterojunctions, functional coupling architectures, pulsed-laser deposition

Contents

S1. Experimental section

Cleaning of Substrates: Before the PLD deposition of materials, ultrasonic treatment is used to remove the remaining contamination on the surface of the SiO_2/Si, Si and sapphire substrates by sequentially immersing them into acetone, ethanol and deionized water. Each cleaning step takes about 15 minutes.

Synthesis of ZIS Nanofilms: High-quality ZIS nanofilms are obtained by PLD deposition and post-growth annealing treatment.

PLD Deposition: A KrF excimer laser (COMPex Pro 110F, Coherent GmbH, Göttingen, Germany, λ = 248 nm) is used for ablating the ZIS target. The pulse number for depositing the ZIS nanofilms is set to be 5000 with the repetition rate of 4 Hz and the operating voltage of 19 kV. The distance between the target and substrate during deposition is approximately 6 cm and the temperature of the substrate holder is set to be 450 ℃ during the ZIS deposition process. The base pressure of the growth chamber is less than 6×10^{-4} Pa, and the growth pressure is set at 40 Pa through aerating 99.99% argon gas at a flow rate of 50 sccm.

Post-Growth Annealing Process: After the PLD deposition, the derived ZIS nanofilms are transferred into a tube furnace (GSL-1100X-S) for annealing treatment. The ZIS nanofilms are set at the middle of the heating zone of the furnace, and the sulfur powder (600 mg, ≥99.95%, Aladdin) is placed on the upstream side of the furnace. To provide a protective gas environment, the tube is flushed with flowing high-purity argon (99.99%) gas for 40 mintues before heating. Then, the furnace temperature is increased to 600 ℃ with a heating rate of 10 ℃/min and is kept at 600 ℃ for 30 minutes. With the assist of the flowing high-purity argon gas, the gasified sulfur species are supplied to the ZIS nanofilms to create a sulfur-rich environment in the furnace.

Synthesis of the SnS/ZIS Heterojunctions: The SnS nanofilms are deposited over the ZIS nanofilms which are obtained by the above two-step process to produce the SnS/ZIS nanofilms. The target is consisted of highly pure SnS_2 powder (99.99%), which is prepared by a sintering process. The pulse number for depositing the SnS nanofilms is set to be 1000, 2000, 3000 and 4000 with the repetition rate of 4 Hz and the operating voltage of 19 kV. The distance between the target and substrate during the PLD deposition is approximately 6 cm, and the temperature of substrate holder is set at

500 ℃ during the deposition process. The base pressure of the growth chamber is less than 6×10^{-4} Pa and the growth pressure is set at 40 Pa through aerating 99.99% argon gas at a flow rate of 50 sccm.

Material Characterizations: The crystal structure of the ZIS, SnS and SnS/ZIS nanofilms are recorded by an XRD system (Rigaku D-MAX 2200 VPC). Raman spectroscopy and PL spectrum measurements are performed at room temperature by a Renishaw InVia spectrometer with an excitation wavelength of 514 nm. The morphology characterizations of the ZIS, SnS and SnS/ZIS nanofilms are achieved by SEM (JSM-6330F). TEM (FEI Tecnai G2 F30) is used to perform further structure and morphology characterizations. The components and structure of the nanofilms are extracted by energy dispersive spectroscopy (EDS) and selected area electron diffraction (SAED) measurements. XPS is recorded with a Thermo Scientific XPS system (Nexsa). The UV-Vis-NIR absorption spectra and reflectance spectra are measured with a UV-Vis-NIR spectrophotometer (Lambda950, Perkin Elmer). An atomic force microscopy system (AFM, Bruker Dimension FastScan) is used to conduct the roughness and thickness measurements.

Device Fabrication: The Ti/Au (10/100 nm) electrode array are patterned onto the nanofilms by photolithography (μPG 501, Heidelberg) and electron beam evaporation (Wavetest, DE400).

Device Characterizations: The measurements of the electrical and photoelectric properties of the devices are carried out on a Lakeshore probe station combined with a semiconductor parameter analyzer (4200-SCS, Keithley). The photoresponse of the photodetectors is measured under 370.6 nm, 405 nm, 532 nm, 671 nm, 808 nm, 1550 nm, 2240 nm lasers in atmospheric environment at room temperature. A high-speed switch is used to generate the pulsed light. A Si photodiode (Throlabs S120VC, for $\lambda \leq$ 808 nm) and a GaInAs photodiode (Throlabs S148C, for $\lambda \geq$ 1550 nm) are exploited to calibrate the laser energy.

Theoretical Methods: The projector-augmented wave pseudopotentials (PAW) were used for relevant calculations, which were based on the Density Functional Theory (DFT) as implemented in the Vienna Ab-initio Simulation Package (VASP) software.[1, 2] The exchange-correlation potential was described by the Perdew-Burke-Ernzerhof (PBE)

in the generalized gradient approximation (GGA).[3, 4] The kinetic energy cutoff for plane-wave expansion was set to 500 eV and the k-point grid in the Brillouin zones (BZ) of pure ZIS, SnS and SnS/ZIS heterojunction by executing Γ-centered $8\times5\times1$, $8\times8\times1$, and $8\times3\times1$,[5] respectively. The full geometry relaxation until the absolute value of all forces was less than 0.01 eV/Å, and the energy convergence threshold for between two sequential steps is 10^{-5} eV. Moreover, The DFT-D3 correction was adopted to rectify the van der Waals interaction between ZIS and SnS layers. The vacuum area of ~25 Å was installed along the *z*-direction to minimize the spurious interactions between the repeating images.

The electronic transport and photocurrent calculations were performed by using the non-equilibrium Green's function (NEGF) combined with DFT within the implemented Atomistix ToolKit (ATK).[6] The energy cutoff of 150 Ry and a k-point mesh of 1 × 1 × 100 were used.[7] The *I-V* curves of ZIS and SnS/ZIS heterojunctions were calculated in terms of the Landauer–Büttiker model:

$$I_\sigma(V_b) = G_0 \int_{\mu_L}^{\mu_R} T_\sigma(E, V_b)\left[f_L(E) - f_R(E)\right] dE, \tag{1}$$

where G_0 stands for the quantum unit of conductance, σ is the spin index and $f_{l(R)}(E)$ is the Fermi distribution function, $T_\sigma(E, V_b)$ represents the transmission coefficient under energy E and bias voltage V_b. A schematic diagram of the electronic device is presented in Fig. S1

In the light of the law of luminous flux conservation,[8] the light absorptance of SnS nanosheets (A_{abs}^{SnS}) and $ZnIn_2S_4$ (A_{abs}^{ZIS}) in tilted/horizontal heterostructures can be described as

$$\begin{cases} A_{abs}^{SnS} = \dfrac{1-R_A}{1-R_A R_B T_1^+ T_1^-}\left(1 - R_B T_1^+ T_1^- - (1-R_B)T_1^+ \dfrac{1 - R_C T_2^+ T_2^- [1-(1-R_B)T_1^-]}{1 - R_B R_C T_2^+ T_2^-}\right) \\ A_{abs}^{ZIS} = \dfrac{(1-R_A)(1-R_B)T_1^+}{1-R_A R_B T_1^+ T_1^-}\left(1 - \dfrac{(1-R_B)R_C T_2^+ T_2^- + (1-R_C)T_2^+}{1 - R_B R_C T_2^+ T_2^-}\right) \end{cases}, \tag{2}$$

where R_A, R_B, R_C are the reflection coefficients at the interfaces of air/SnS, SnS/ZIS and air/ZIS, respectively.

$$R_A = (n_{air} - n_{SnS}^*)^2 / (n_{air} + n_{SnS}^*)^2, \tag{3}$$

$$R_B = (n_{SnS} - n_{ZIS})^2 / (n_{SnS} + n_{ZIS})^2, \tag{4}$$

$$R_C = (n_{ZIS} - n_{air})^2 / (n_{ZIS} + n_{air})^2, \tag{5}$$

$$n_{SnS}^{*} = n_{air} + \frac{HD}{L(H\sin\theta + D\cos\theta)}(n_{SnS} - n_{air}), \tag{6}$$

n_{SnS}^{*} is the effective refractive index of nanosheet array, θ is the tilt angle of SnS nanosheets, *H* and *D* are the height of SnS and the thickness of ZIS, and *L* is the array periodicity of SnS nanosheets, i.e., the distance between two adjacent nanosheets, n_{air}, n_{SnS} =1.25 and n_{ZIS} =2.50 are the refractive index of air, SnS and ZIS.[9, 10] T_1^{+} (T_2^{+}) and T_1^{-} (T_2^{-}) are the fraction of downward flux transmitted to the rear surface of SnS nanosheets (ZIS) and that of light reflected from the rear that is transmitted to the front surface of SnS nanosheets (ZIS), respectively. Physically, the fraction of luminous flux is

$$\begin{cases} T_1^{\pm} = 1 - \Gamma\left[1 - \exp\left(-\alpha_{SnS}(\lambda)(H\sin\theta + D\cos\theta)\right)\right] \\ T_2^{\pm} = \exp\left(-\alpha_{ZIS}(\lambda)D\right) \end{cases}, \tag{7}$$

where Γ is the ratio of effective-to-actual illumination area, it is expressed as

$$\Gamma = \left(H\cos\theta + D\sin\theta\right)/L \tag{8}$$

α_{SnS} and α_{ZIS} are the light absorption coefficients of SnS nanosheets and ZIS that can be calculated by Tauc's law

$$\alpha = A_{\alpha}^{*}\left(h\nu - E_g\right)^{\Omega}/h\nu, \tag{9}$$

where A_{α}^{*} and $h\nu$ being the Tauc constant and incoming photon energy in the Tauc's law, respectively. $\Omega = 1/2$ for indirect transition and $\Omega = 2$ for direct transition[11]. The necessary parameters $A_{\alpha}^{*} = 2.17\times10^{5}$ ($A_{\alpha}^{*} = 2.57\times10^{4}$) for SnS (ZIS) are obtained from refs [12] and [13]. Therefore, the total light absorptance in SnS/ZIS heterostructures can be obtained as

$$A_{abs} = A_{abs}^{SnS} + A_{abs}^{ZIS} \tag{10}$$

S2. Characterizations of crystal structure and element valance states the pristine SnS produced by PLD

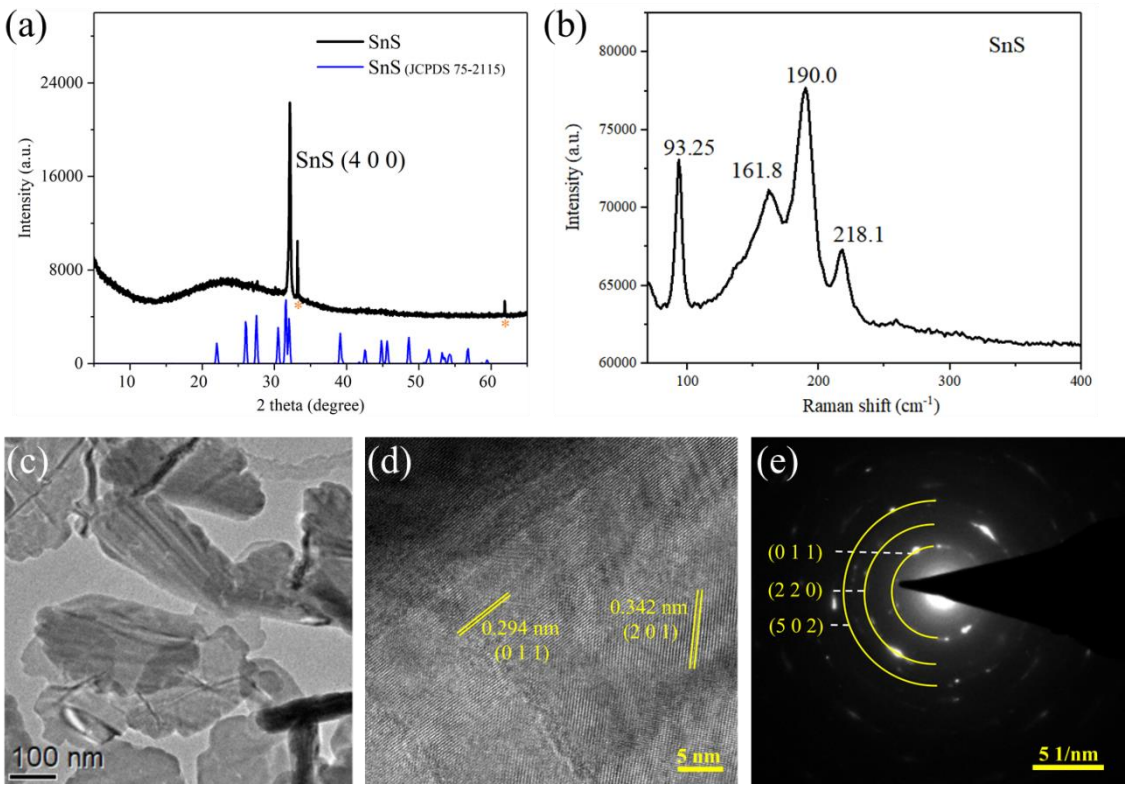

Fig. S1 Characterizations of the PLD-derived SnS. (a) 2θ–ω XRD pattern. The stars mark the diffraction peaks from the Si substrate. (b) Raman spectrum under 514 nm laser excitation. (c) Low-magnification TEM image. (d) High-resolution TEM image. (e) SAED pattern.

S3. Component characterizations of the pristine SnS produced by PLD

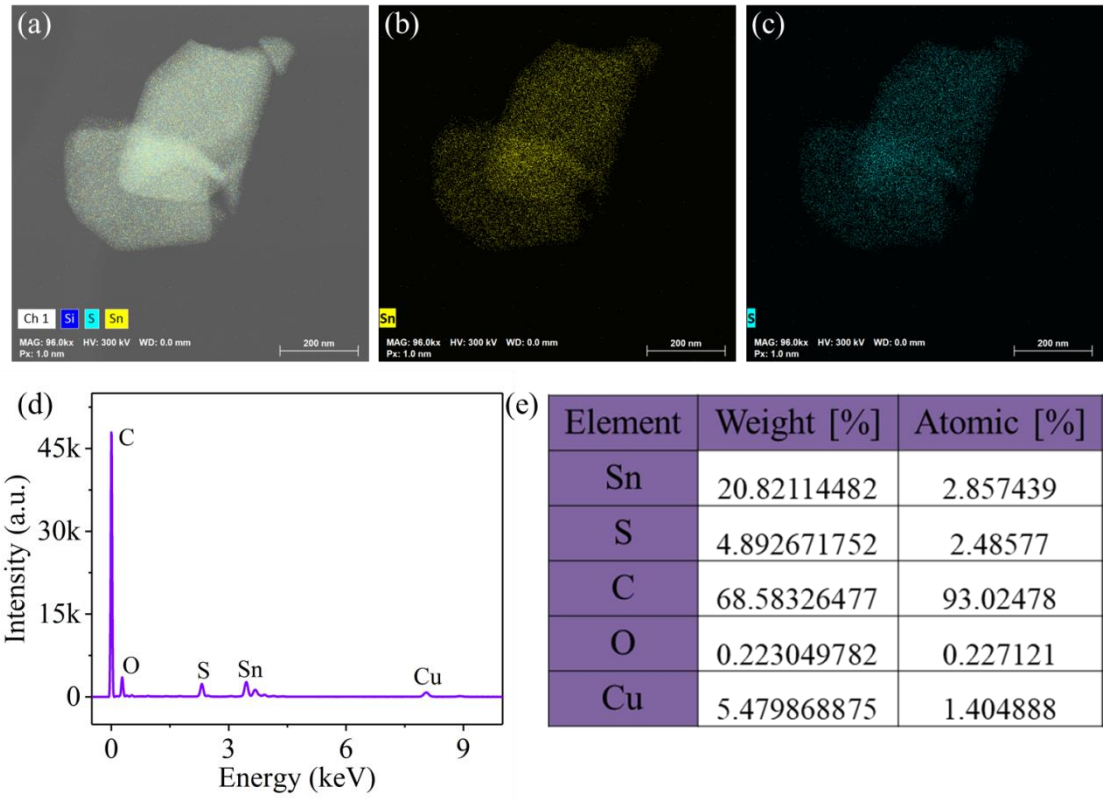

(e)

Element	Weight [%]	Atomic [%]
Sn	20.82114482	2.857439
S	4.892671752	2.48577
C	68.58326477	93.02478
O	0.223049782	0.227121
Cu	5.479868875	1.404888

Fig. S2 (a) Low-magnification TEM image and the corresponding element mapping images of (b) Sn and (c) S elements. (d) EDS spectrum and (e) a summary of the corresponding element compositions.

S4. Fabrication process for preparing the SnS/ZIS hierarchical heterostructure

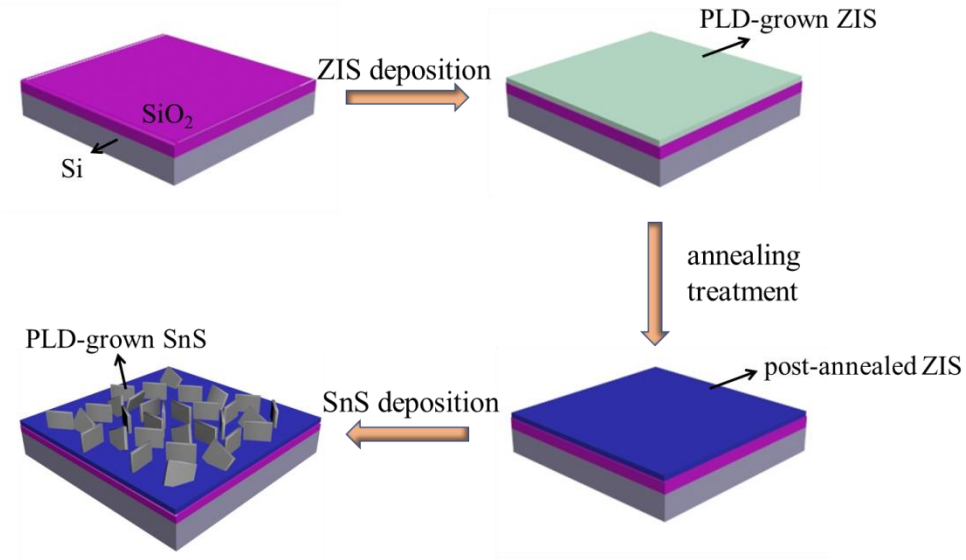

Fig. S3 Schematic illustration of the fabrication procedures for constructing SnS/ZIS *via* PLD.

S5. SEM morphology of the PLD-derived SnS/ZIS hierarchical heterostructure

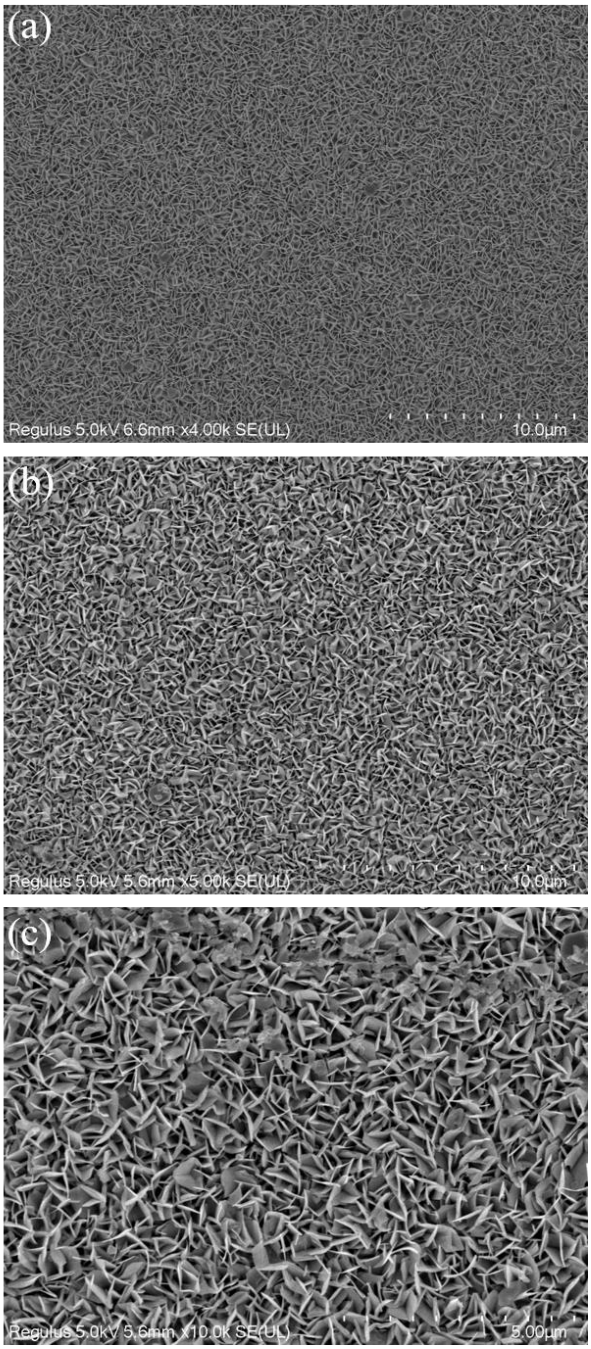

Fig. S4 SEM images of the PLD-derived SnS/ZIS hierarchical heterostructure. (a) 4000×, (b) 5000×, (c) 10000×.

S6. Crystalline orientation of the PLD-derived SnS on a SiO_2/Si substrate

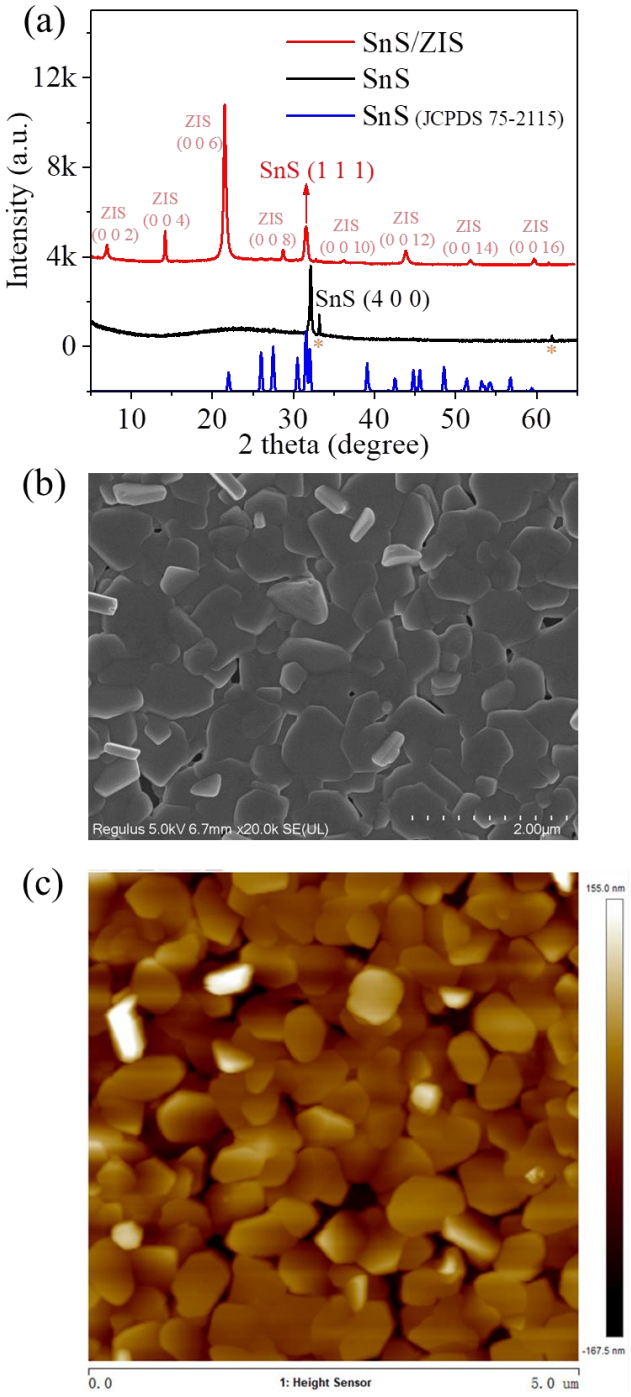

Fig. S5 (a) XRD patterns of the PLD-grown SnS (black line) and SnS/ZIS (red line) nanofilms. (b) SEM image (20000×) and (c) AFM image of the SnS grown on a SiO_2/Si substrate. The theoretical diffraction peaks of SnS are also included in (a) for comparison (blue line). Evidently, the SnS grown on a SiO_2/Si substrate is horizontally aligned, which is different from that grown on ZIS.

S7. Comparison of the surface roughness of the PLD-derived ZIS nanofilm and the SiO_2/Si substrate

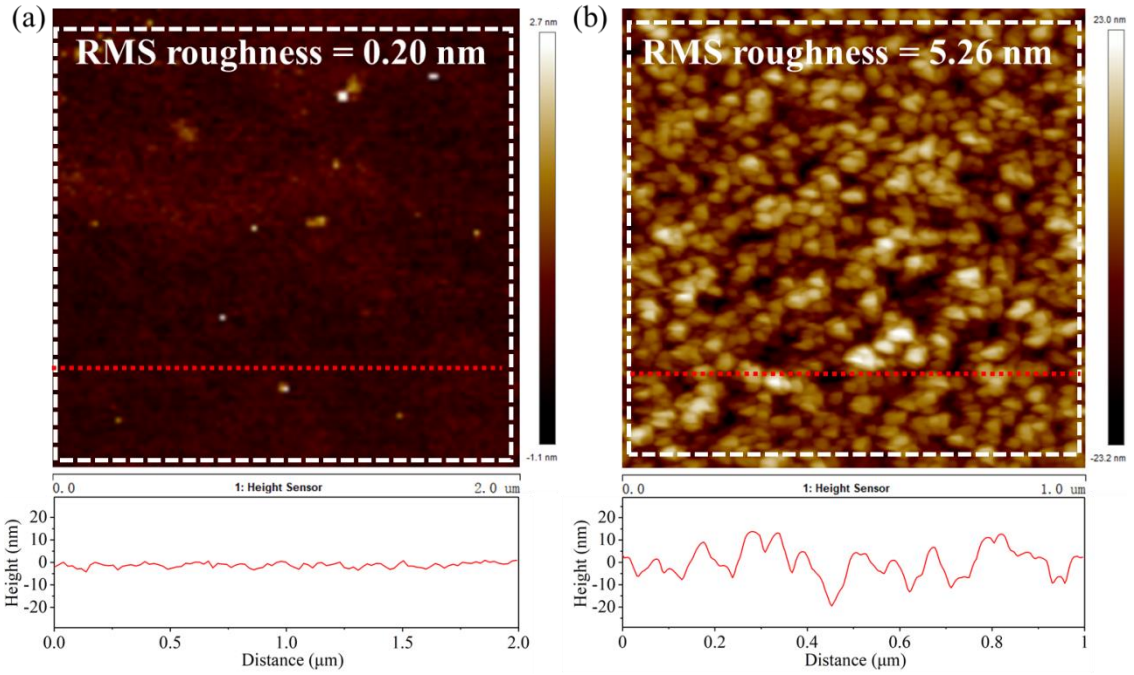

Fig. S6 AFM images of (a) a bare SiO_2/Si substrate and (b) a PLD-derived ZIS nanofilm. The bottom images present the corresponding line scans marked in the upper images. It is evident that the surface becomes much rougher after the deposition of ZIS nanofilm.

S8. Comparison of the reflectivity of the PLD-derived ZIS, SnS and SnS/ZIS nanofilms

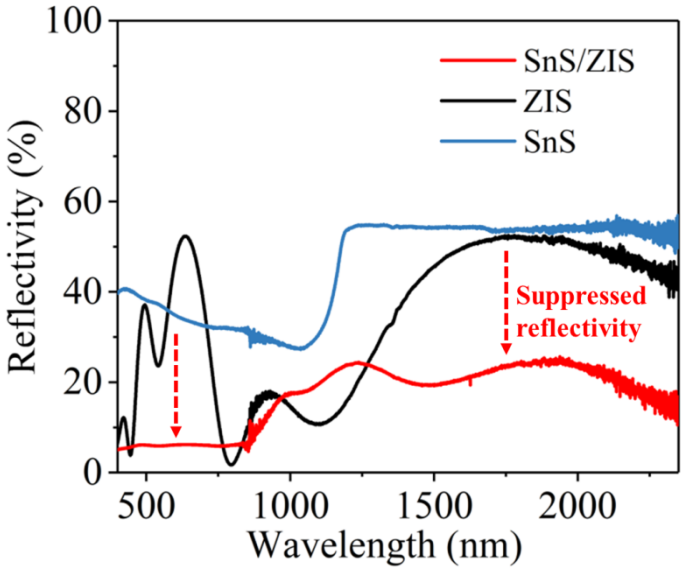

Fig. S7 Reflection spectra of the PLD-derived ZIS (black line), SnS (blue line) and SnS/ZIS (red line) nanofilms. The reflectivity of the SnS/ZIS nanofilm is largely suppressed (marked by the red arrows) as compared to the SnS and ZIS nanofilms.

S9. Morphology of the PLD-derived SnS/ZIS hierarchical heterostructure

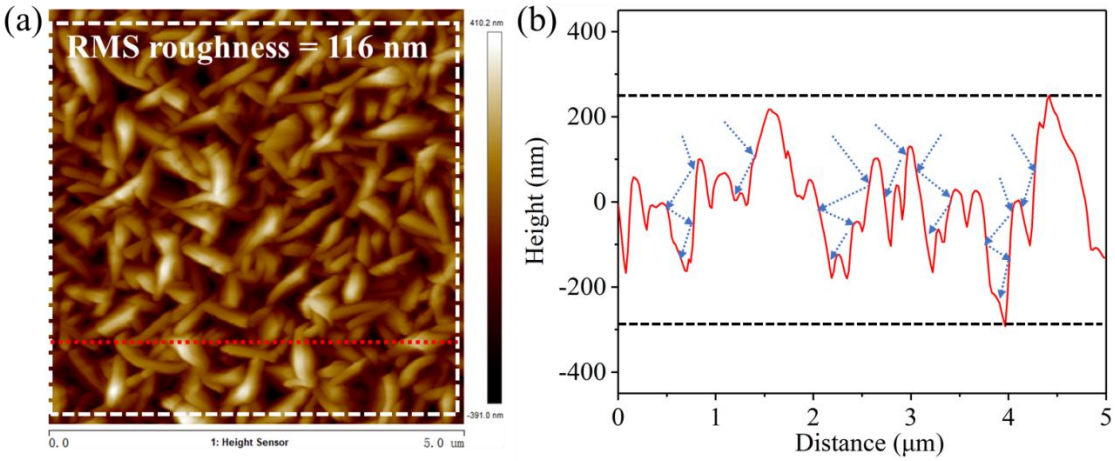

Fig. S8 (a) AFM image of the PLD-derived SnS/ZIS hierarchical heterostructure and (b) the corresponding height profile along the red dash line. The RMS roughness reaches up to ≈116 nm, which is ≈22 times of that of pristine ZIS. The maximum crest-to-valley amplitude exceeds 500 nm. The blue dash arrows indicate the light-trapping process.

S10. Schematic diagram illustrating the increase of reflectivity of SnS/ZIS at long wavelengths

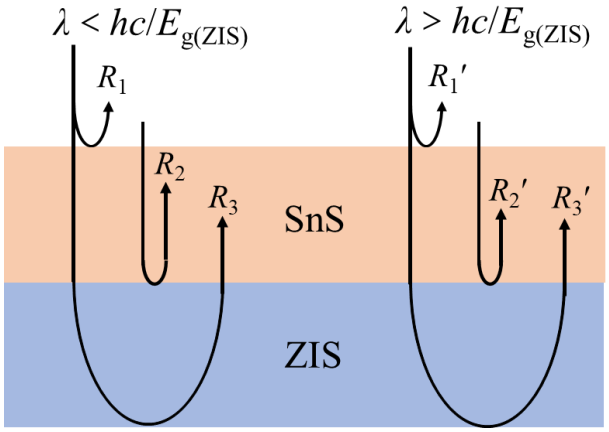

Fig. S9 Schematic diagram illustrating the increase of reflectivity of the PLD-derived SnS/ZIS hierarchical nanofilm at long wavelengths. Herein, R_1, R_2 and R_3 represent the reflected light with wavelength below $hc/E_{g(ZIS)}$ (h is the Planck constant, c is the light velocity, and $E_{g(ZIS)}$ is the bandgap of ZIS) at the air/SnS, SnS/ZIS and ZIS/substrate interfaces, while R_1', R_2' and R_3' represent the reflected light with wavelength beyond $hc/E_{g(ZIS)}$ at the air/SnS, SnS/ZIS and ZIS/substrate interfaces.

S11. Power density dependent photocurrent of the ZIS and SnS/ZIS photodetectors upon various illuminations

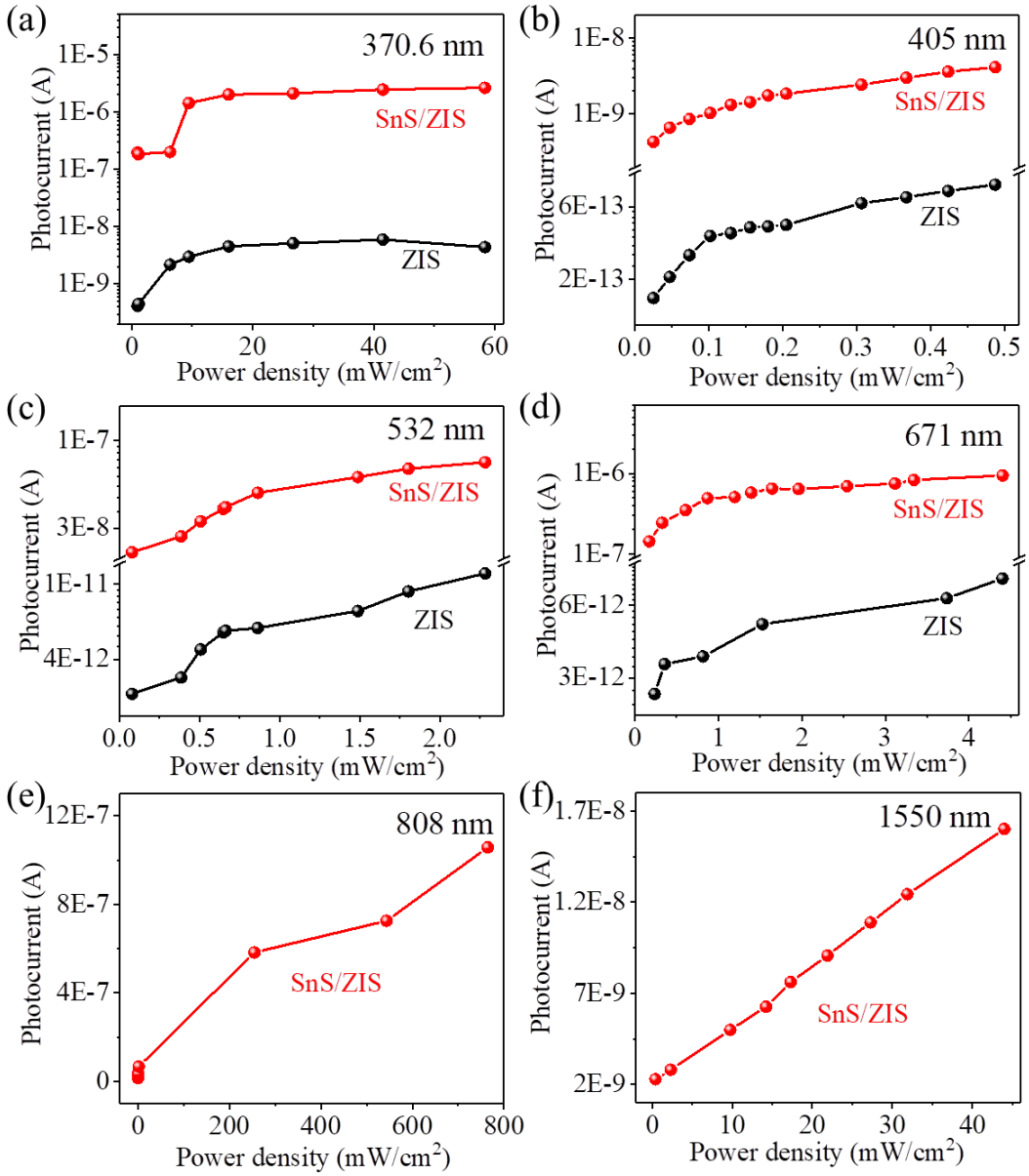

Fig. S10 Photocurrent as a function of the light power density of the ZIS and SnS/ZIS photodetectors upon (a) 370.6 nm, (b) 405 nm, (c) 532 nm, (d) 671 nm, (e) 808 nm and (f) 1550 nm illuminations. Upon long-wavelength illuminations (808 and 1550 nm), the ZIS photodetector exhibits no photoresponse.

S12. Definition of responsivity, EQE, detectivity, and rise/decay time

To evaluate the photosensitivity of photodetectors, several pivotal figures-of-merit have been developed, including responsivity (R), EQE and detectivity (D^*). Responsivity is equal to the photocurrent generated upon light illumination with per unit power. It can be calculated according to the following formula

$$R = \frac{I_{\text{light}} - I_{\text{dark}}}{PS}, \tag{10}$$

where I_{light} is the channel current under light illumination, I_{dark} is the channel current in dark condition, P is the power density of incident light, and S is the photosensitive area of the photodetector. EQE refers to the ratio of the number of photocarriers crossing the photosensitive channel to the number of incident photons onto the photosensitive area. It can be calculated according to the following formula

$$\text{EQE} = \frac{I_{\text{light}} - I_{\text{dark}}}{e} / \left(\frac{PS}{hv} \right) = \frac{hcR}{\lambda e}, \tag{11}$$

where h is the Planck constant, v is the light frequency, c is the light speed, λ is the wavelength of incident light, e is the elemental charge. Detectivity is a performance metric used to evaluate the capability of photodetectors to distinguish weak light signals. It is calculated according to the following formula

$$D^* = \frac{\sqrt{S}R}{\sqrt{2eI_{\text{dar}}}}. \tag{12}$$

Response rate is commonly evaluated by the rise time and decay time during photoswitching. They are defined as the time intervals required for the photocurrent to rise from 0% to 90% and to decay from 100% to 10%, respectively.

S13. Power density dependent EQE of the ZIS and SnS/ZIS photodetectors upon various illuminations

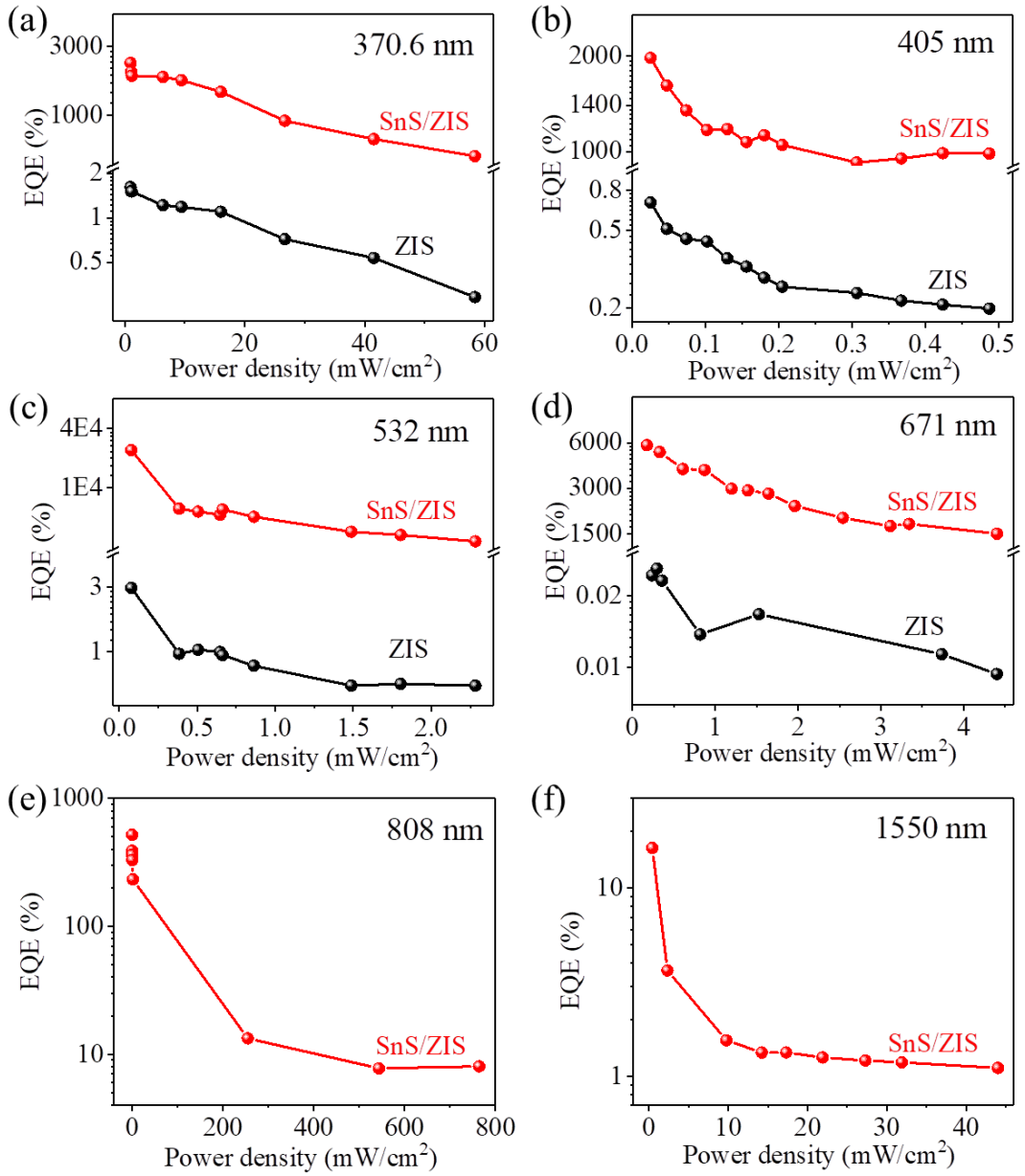

Fig. S11 EQE as a function of the power density of the ZIS and SnS/ZIS photodetectors upon (a) 370.6, (b) 405, (c) 532, (d) 671, (e) 808 and (f) 1550 nm illuminations. Upon long-wavelength illuminations (808 and 1550 nm), the ZIS photodetector exhibits no photoresponse.

S14. Power density dependent detectivity of the ZIS and SnS/ZIS photodetectors upon various illuminations

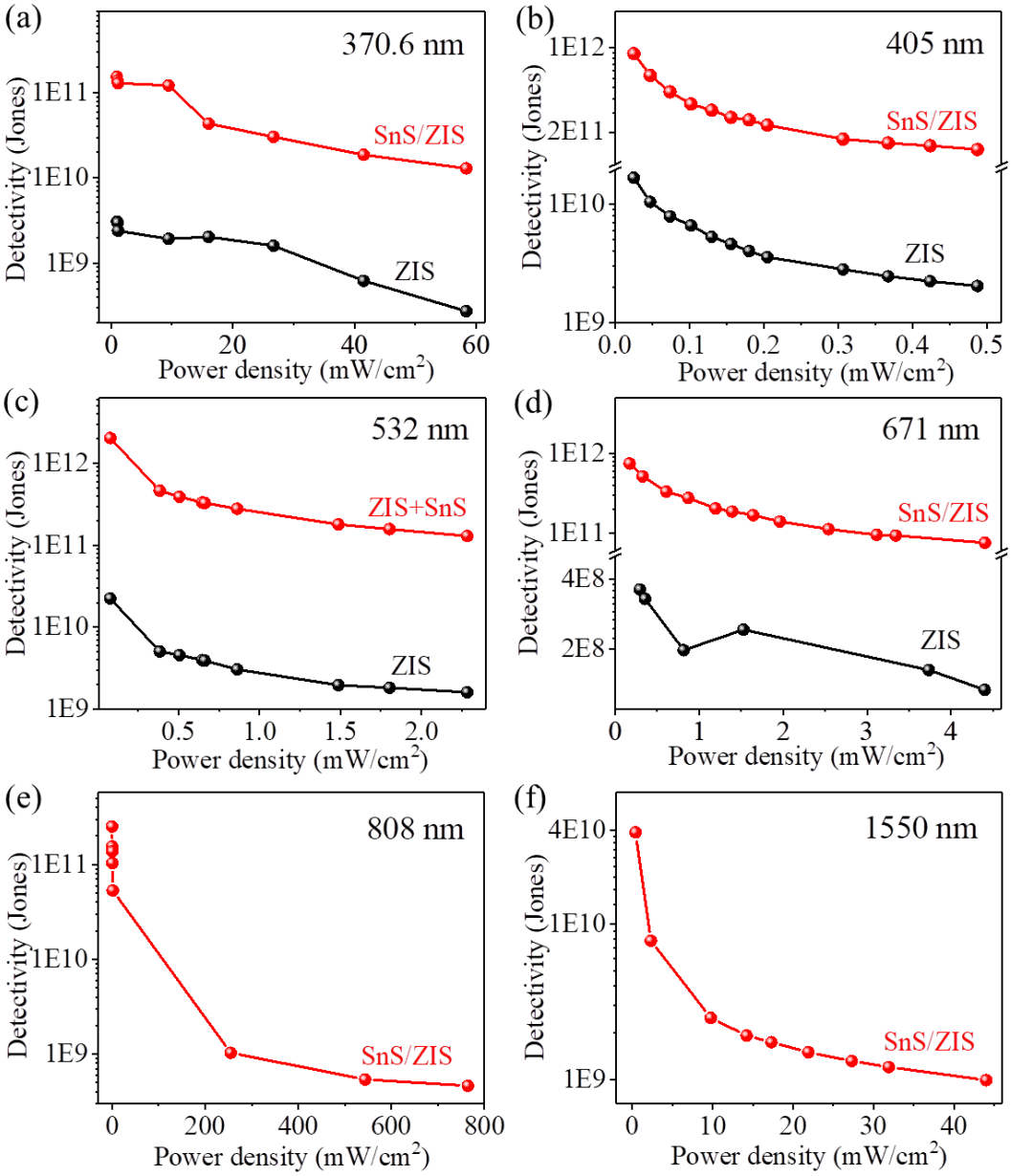

Fig. S12 Detectivity as a function of the power density of the ZIS and SnS/ZIS photodetectors upon (a) 370.6, (b) 405, (c) 532, (d) 671, (e) 808 and (f) 1550 nm illuminations. Upon long-wavelength illuminations (808 and 1550 nm), the ZIS photodetector exhibits no photoresponse.

S15. Photoswitching curves of the ZIS and SnS/ZIS photodetectors upon infrared illuminations

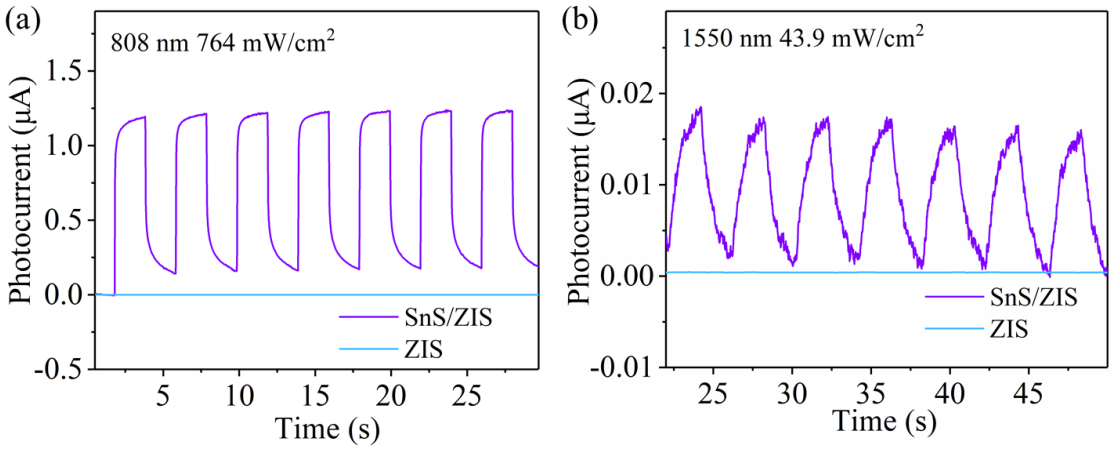

Fig. S13 Photoswitching curves of the pristine ZIS photodetector (wathet blue lines) and the SnS/ZIS photodetector (purple lines) upon (a) 808 and (b) 1550 nm periodic illuminations.

S16. Comparison of the spectral photoresponse of the ZIS and SnS/ZIS photodetectors

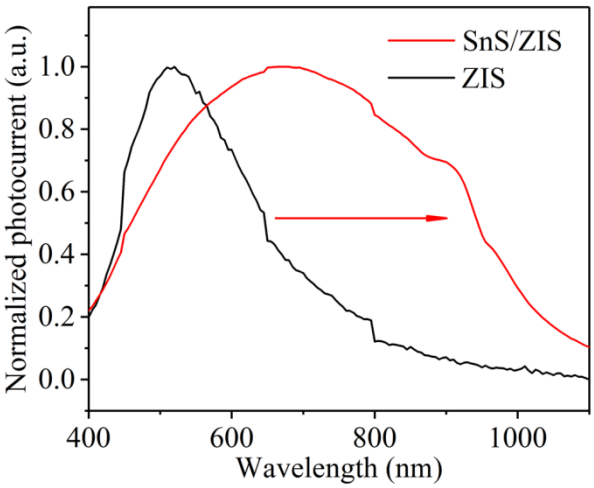

Fig. S14 Spectral photoresponse curves of the PLD-derived ZIS (black) and SnS/ZIS (red) photodetectors. It is evident that the effective optical window has been substantially extended to the long-wavelength region (marked by the red arrow) after the integration of SnS onto ZIS.

S17. Comparison of the enhancement factors of this study with state-of-the-art improvement strategies on 2DLM photodetectors

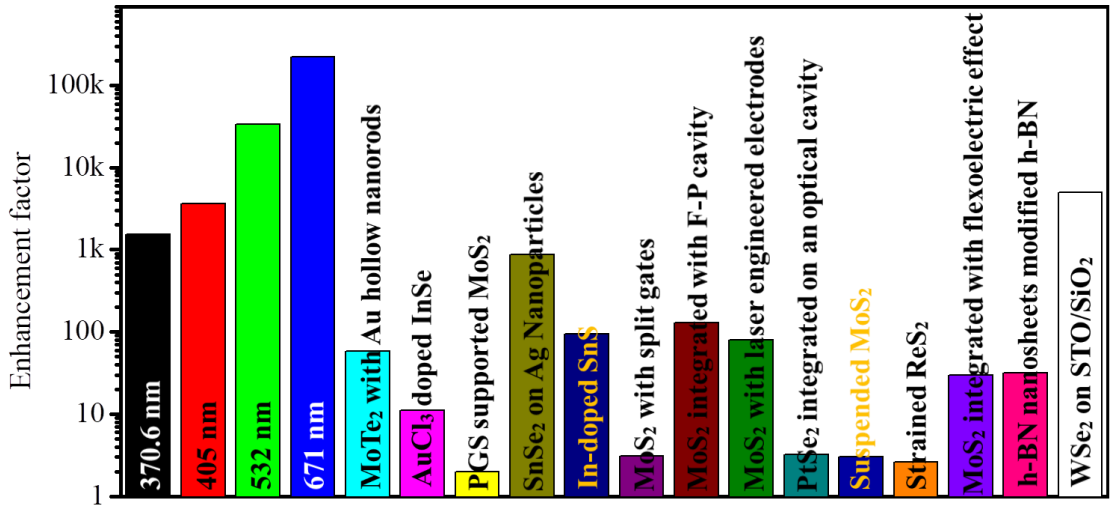

Fig. S15 A summary of the enhancement factors of our SnS/ZIS photodetector and the state-of-the-art improvement strategies on 2D material photodetectors.[14-27]

S18. Response rate of a SnS/ZIS photodetector

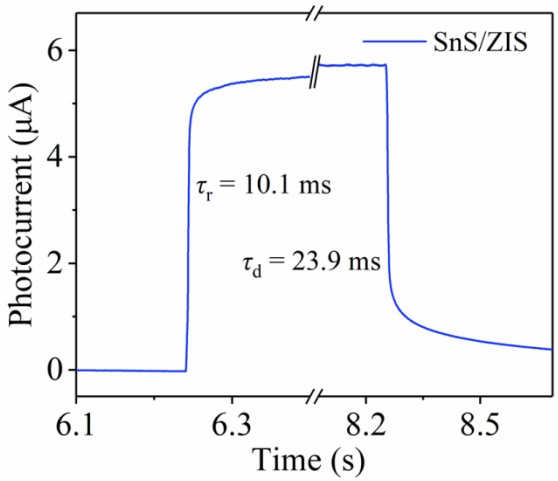

Fig. S16 Rise and fall edges of a SnS/ZIS photodetector.

S19. Comparison of the figures-of-merit of the SnS/ZIS photodetectors with state-of-the-art 2DLM based photodetectors

Table S1. A summary of the operating voltage (V_{ds}), responsivity, EQE, detectivity, effective wavelength range and response/recovery time of the SnS/ZIS photodetectors and state-of-the-art 2DLM based photodetectors.

Materials	V_{ds} (V)	R (A/W)	EQE (%)	D^* (Jones)	τ_r/τ_d (ms)	Wavelength (nm)	Ref.
SnS/ZIS	**2**	**103.7**	**2.4×10^4**	**2.03×10^{12}**	**10.1/23.9**	**370–1550**	**Ours**
WS_2	10	0.144	N/A[a)]	10^8	0.07	400–800	28
$TaIrTe_4$	N/A	0.13	4.03	N/A	N/A	633–4000	29
GaS	20	4.7	1312	1.4×10^{12}	<66	275–532	30
$CuInP_2S_6$	4	0.0108	4.78	7.38×10^{10}	0.36/0.44	280–520	31
$InSiTe_3$	11	0.0709	N/A	7.59×10^9	$\approx5\times10^4$	365–1310	32
Si_2Te_3	1	65	1.99×10^4	2.81×10^{12}	210/478	405–1064	33
$SnSe_2$/AgNPs[b)]	0.1	0.194	59.4	8.4×10^9	21	405–2200	17
SiAs	2	0.016	1200	1×10^{10}	3000/1500	325–514.5	34
SiP	N/A	≈18	6115	$\approx2.25\times10^{11}$	0.06/0.03	300–700	35
$In_{4/3}P_2Se_6$	5	4.31	1485.2	6.3×10^{12}	0.47/0.44	360–639	36
Au_2P_3	N/A	0.97	77.6	2.9×10^{10}	1440/1340	1550–2611	37
$MoTe_2$	−2	0.5	37	N/A	N/A	1550	38
WSe_2	2	170	3962	1.1×10^{12}	0.014	432	19
$PtSe_2$	0.05	0.054	8.02	2.5×10^6	5.4×10^{-5}	532–8350	22
MoS_2/PSS[c)]	20	8.8×10^{-3}	3	1.2×10^{10}	2240/2270	365–660	23
h-BN/AuNPs[d)]	35	2.24×10^{-5}	0.14	N/A	N/A	205–390	26
MoS_2/Au Array	5	13	N/A	N/A	N/A	532–1550	39

a) N/A: Not applicable. b) AgNPs: Ag nanoparticles.

c) PSS: Patterned sapphire substrate. d) AuNPs: Au nanoparticles.

S20. Comparison of the figures-of-merit of the SnS/ZIS photodetectors with state-of-the-art 2DLM based heterojunction photodetectors

Table S2. A summary of the operating voltage (V_{ds}), responsivity, EQE, detectivity, effective wavelength range and response/recovery time of the SnS/ZIS photodetectors and state-of-the-art 2DLMs based heterojunction photodetectors.

Heterostructures	V_{ds} (V)	R (A/W)	EQE (%)	D^* (Jones)	τ_r/τ_d (ms)	Wavelength (nm)	Ref.
SnS/ZIS	**2**	**103.7**	**2.4×10^4**	**2.03×10^{12}**	**10.1/23.9**	**370–1550**	**Ours**
Sn/InSe	0	0.032	8.7	1.7×10^{11}	30/37	300–700	40
MoS_2 QDs[a)]/MoS_2	2	0.0128	2.86	7.2×10^9	2740	UV-vis-NIR	41
$PtSe_2$/Gr[b)]	0.02	0.4	76.5	$\approx10^7$	50.6/37.3	637–10600	42
Te/MoS_2	0.8	28.4	5700	2.7×10^{10}	N/A[c)]	980–3000	43
PtS_2/WSe_2	1	1.7	≈3320	3.8×10^{10}	0.008/0.009	400–800	44
Te/ReS_2	1	180	≈35316	7.2×10^9	5/8	632	45
WS_2/$GaS_{0.87}$	2	25	≈4984	1.5×10^9	5000	395–622	46
WO_x/WSe_2	2	3663	N/A	N/A	50	White light	47
WSe_2/WS_2	N/A	300	6.99×10^4	4.3×10^{10}	1.46/1.42	532	48
$MoTe_2$/Gr	−0.1	0.2	19.08	N/A	19×10^{-9}	1265–1330	49
$CuInSe_2$/In_2Se_3	0	0.01052	3.22	N/A	195/180	405–1310	50
Bi_2Se_3/BP[d)]	0.1	0.0121	≈1.58	N/A	1.3/8.4	350–950	51
MoS_2/Si	6	0.01007	≈1.46	4.53×10^{10}	0.078/0.076	850	52
Bi_2O_2Se/$CsPbBr_3$	3	46	≈9200	2.73×10^{10}	0.012/0.028	390–840	53
Te/Bi_2O_2Se	0.1	130	≈30300	2.5×10^{11}	0.33/0.43	405–635	54
InSe/$NbTe_2$	2	84	≈19579	N/A	< 10	532	55
$Cs_2AgBiBr_6$/WS_2/Gr	4	0.054	≈14.7	1.13×10^{12}	0.0523/0.0536	360–660	56

a) QDs: quantum dots. b) Gr: graphene. c) N/A: Not applicable.

d) BP: black phosphorus.

S21. Bandgap values of ZIS and SnS deduced from the absorption spectra

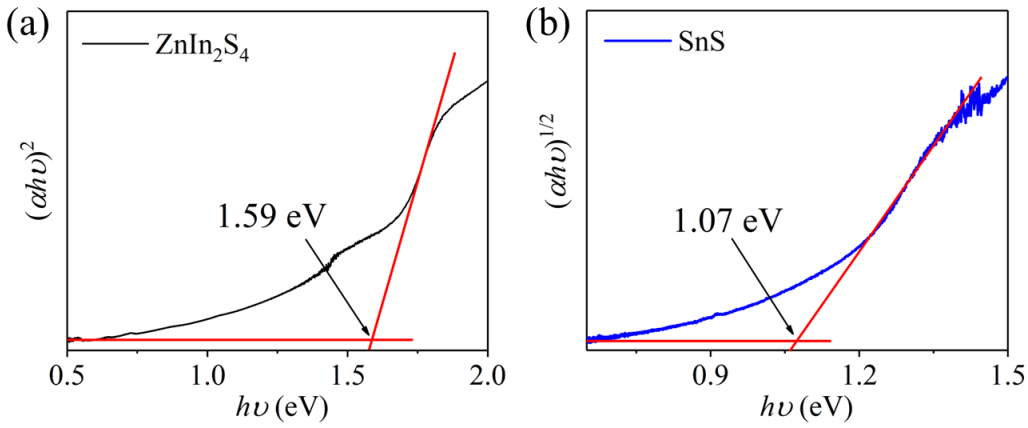

Fig. S17 Tauc plots of the absorption spectra of the PLD-derived (a) ZIS and (b) SnS nanofilms.

S22. Band alignment of the PLD-derived ZIS and SnS

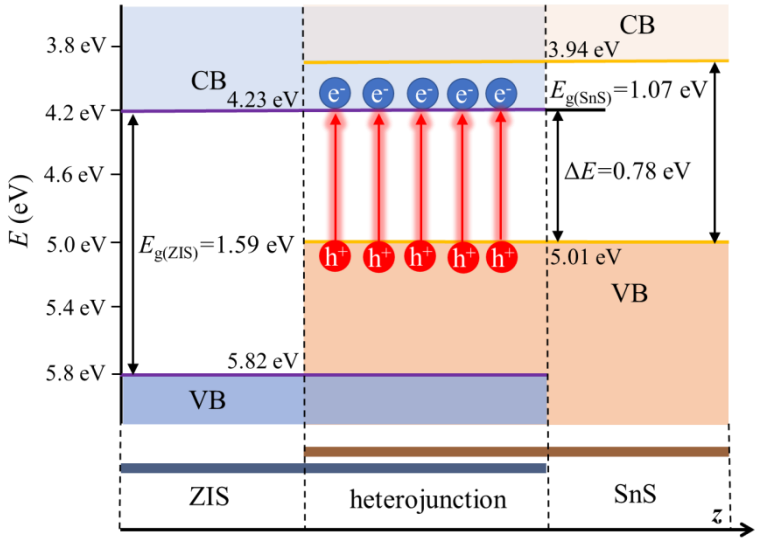

Fig. S18 Band alignment of the PLD-derived ZIS and SnS deduced from the UPS and absorption spectra results. The red arrows represent interlayer excitation. Red balls: holes. Blue balls: electrons. CB: conduction band. VB: valence band. $E_{g(ZIS)}$: bandgap of ZIS. $E_{g(SnS)}$: bandgap of SnS. ΔE: bandgap of SnS/ZIS heterojunction.

S23. Photoresponse of the SnS/ZIS photodetector to 2240 nm illumination

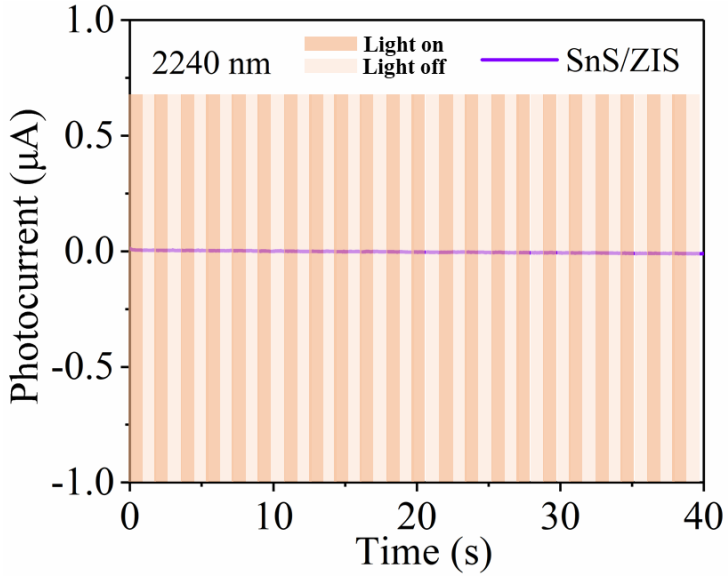

Fig. S19 Photocurrent as a function of time of the SnS/ZIS photodetector under periodic 2240 nm illumination. No discernable photoresponse is observed.

S24. The effect of the laser pulse number of SnS on the density of the SnS nanosheets

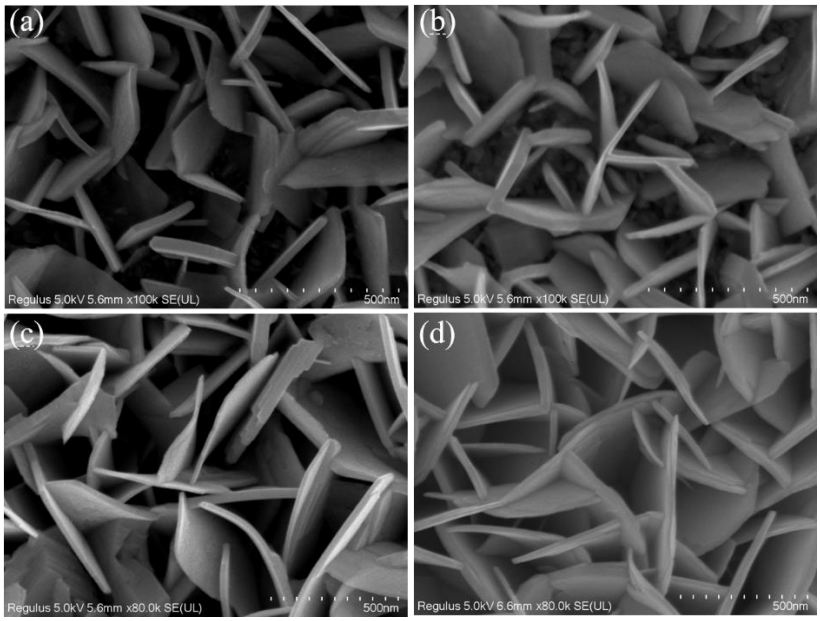

Fig. S20 SEM images of the PLD-derived SnS/ZIS hierarchical heterostructure with the pulse number of SnS of (a) 1000, (b) 2000, (c) 3000, and (d) 4000, respectively.

S25. The effect of the pulse number of SnS on the photoresponse of the SnS/ZIS photodetectors

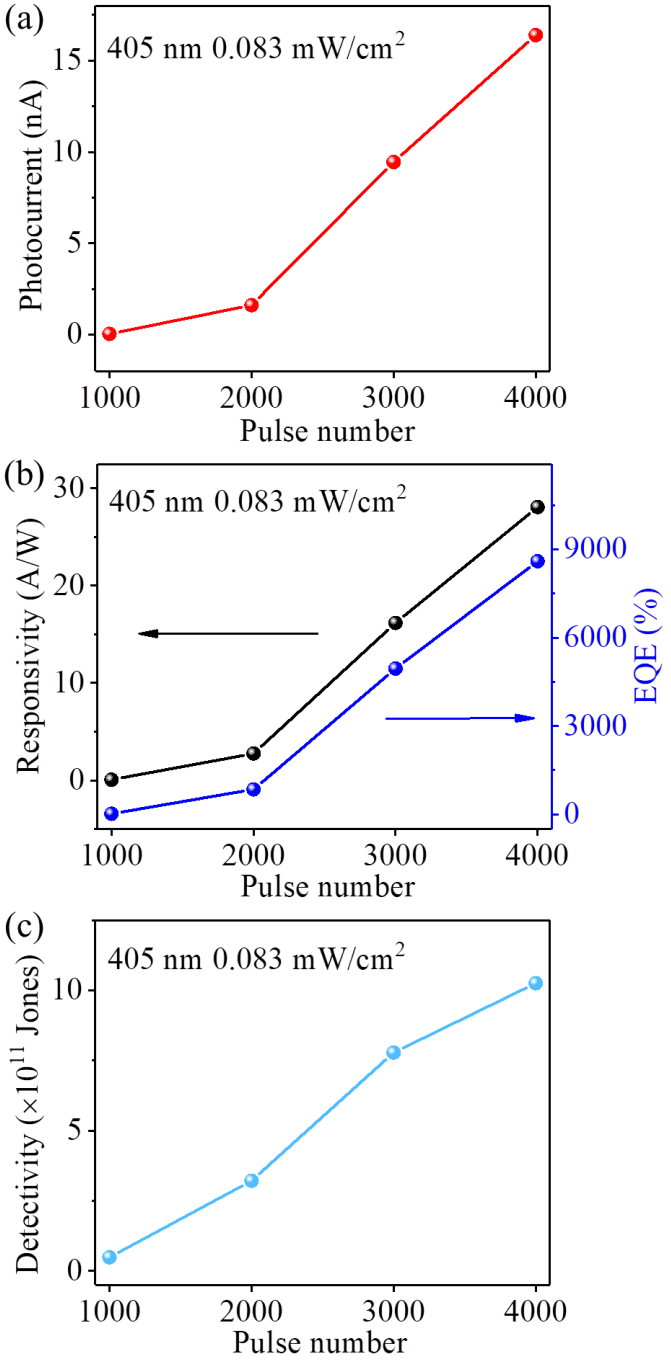

Fig. S21 (a) Photocurrent, (b) responsivity (black line) and EQE (blue line), and (c) detectivity as a function of the laser pulse number of the PLD-derived SnS/ZIS photodetectors.

S26. Theoretical band structures of ZIS and SnS

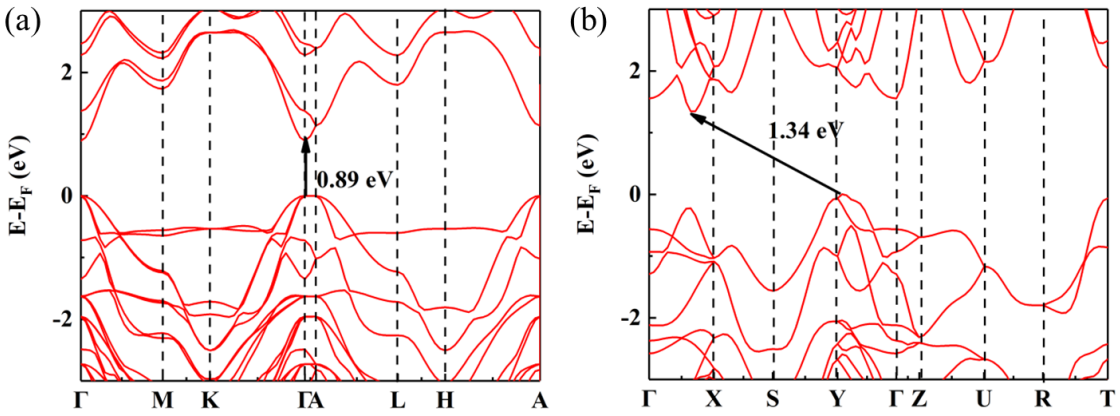

Fig. S22 Band structures of (a) bulk ZIS and (b) bulk SnS based on the framework of HSE06.

S27. Evaluation of the uniformity of the wafer-scale SnS/ZIS nanofilm

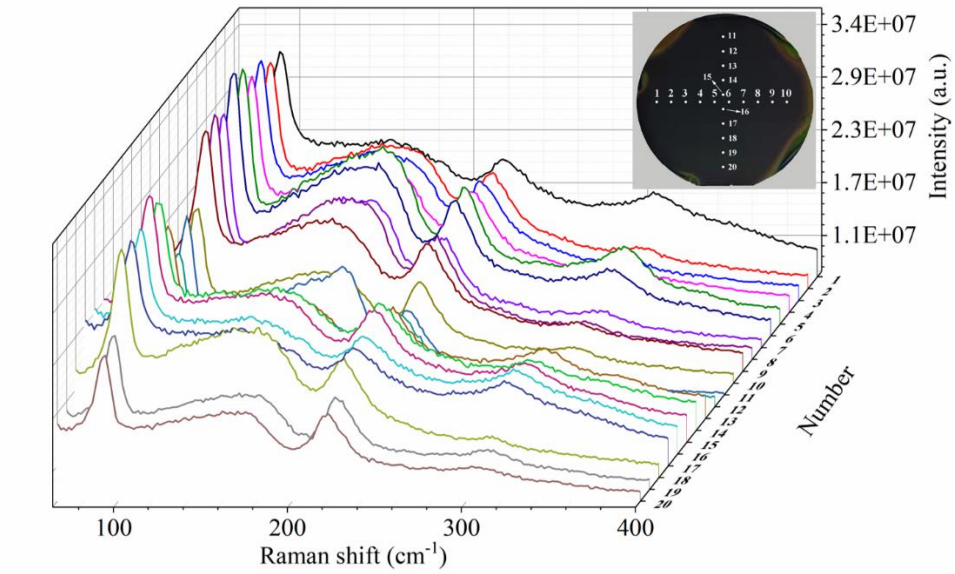

Fig. S23 A summary of the Raman spectra of random 20 points across the PLD-derived wafer-scale SnS/ZIS nanofilm upon 514 nm laser excitation. The inset presents the digital photograph marking the tested points.

S28. Optical imaging based on the SnS/ZIS photodetectors under various illuminations

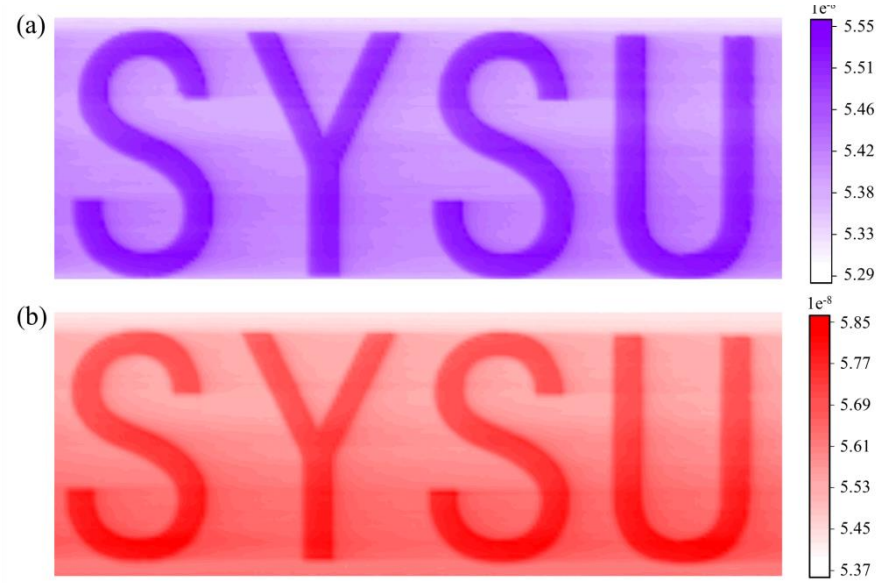

Fig. S24 Imaging results of the "SYSU" pattern by the SnS/ZIS photodetectors under (a) 405 (bluish violet) and (b) 635 nm (red) illuminations.

S29. Stability of the PLD-derived SnS/ZIS nanofilm

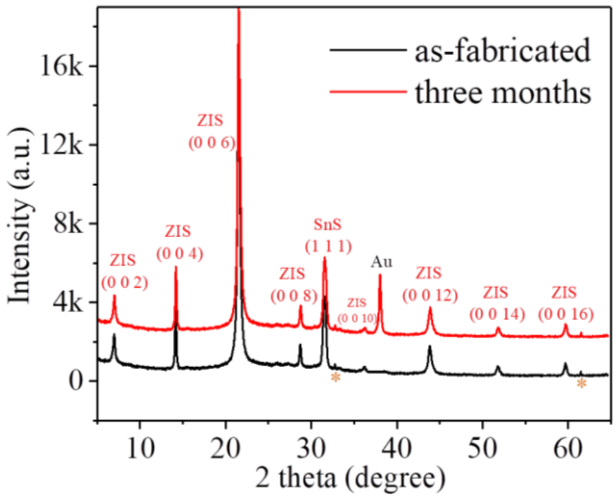

Fig. S25 XRD patterns of the as-fabricated SnS/ZIS nanofilm (black line) and that after storage in the ambient environment for 3 months (red line). All the diffraction peaks from both ZIS and SnS are well maintained.

References

1. G. Kresse and J. Hafner, *Phys. Rev. B*, 1993, **47**, 558–561.
2. G. Kresse, J. Furthmüller and J. Hafner, *Phys. Rev. B*, 1994, **50**, 13181–13185.
3. J. P. Perdew, K. Burke and M. Ernzerhof, *Phys. Rev. Lett.*, 1996, **77**, 3865–3868.
4. J. P. Perdew, K. Burke and M. Ernzerhof, *Phys. Rev. Lett.*, 1998, **80**, 891–891.
5. S. Grimme, *J. Comput. Chem.*, 2006, **27**, 1787–1799.
6. M. Brandbyge, J. L. Mozos, P. Ordejón, J. Taylor and K. Stokbro, *Phys. Rev. B*, 2002, **65**, 165401.
7. D. Xu, L. Hou, J. Dong, H. Hu and G. Ouyang, *Phys. Status Solidi RRL*, 2021, **15**, 2100390.
8. M. A. Green, *Prog. Photovoltaics*, 2002, **10**, 235–241.
9. H. Kafashan, M. Azizieh and Z. Balak, *Appl. Surf. Sci.*, 2017, **410**, 186–195.
10. M. Yousaf, F. Inam, R. Khenata, G. Murtaza, A. R. M. Isa and M. A. Saeed, *J. Alloys Compd.*, 2014, **589**, 353–363.
11. S. Mirabella, R. Agosta, G. Franzò, I. Crupi, M. Miritello, R. L. Savio, M. A. D. Stefano, S. D. Marco, F. Simone and A. Terrasi, *J. Appl. Phys.*, 2009, **106**, 103505.
12. H. S. Yun, B. W. Park, Y. C. Choi, J. Im, T. J. Shin and S. I. Seok, *Adv. Energy Mater.*, 2019, **9**, 1901343.
13. M. Xiong, B. Chai, J. Yan, G. Fan and G. Song, *Appl. Surf. Sci.*, 2020, **514**, 145965.
14. J. You, Y. Yu, K. Cai, D. Zhou, H. Zhu, R. Wang, Q. Zhang, H. Liu, Y. Cai, D. Lu, J. K. Kim, L. Gan, T. Zhai and Z. Luo, *Nano Res.*, 2020, **13**, 1636–1643.
15. H. Jang, Y. Seok, Y. Choi, S. H. Cho, K. Watanabe, T. Taniguchi and K. Lee, *Adv. Funct. Mater.*, 2020, **31**, 2006788.

16. X. Liu, S. Hu, Z. Lin, X. Li, L. Song, W. Yu, Q. Wang and W. He, *ACS Appl. Mater. Interfaces*, 2021, **13**, 15820–15826.

17. X. Sun, J. Sun, J. Xu, Z. Li, R. Li, Z. Yang, F. Ren, Y. Jia and F. Chen, *Small*, 2021, **17**, 2102351.

18. C. Fan, Z. Liu, S. Yuan, X. Meng, X. An, Y. Jing, C. Sun, Y. Zhang, Z. Zhang, M. Wang, H. Zheng and E. Li, *ACS Appl. Mater. Interfaces*, 2021, **13**, 35889–35896.

19. S. Ghosh, A. Varghese, K. Thakar, S. Dhara and S. Lodha, *Nat. Commun.*, 2021, **12**, 3336.

20. X. Chen, X. Yang, Q. Lou, Y. Zhang, Y. Chen, Y. Lu, L. Dong and C. X. Shan, *Nano Res.*, 2021, 10.1007/s12274-12021-13989-12274.

21. J. Huo, Y. Xiao, T. Sun, G. Zou, D. Shen, B. Feng, L. Lin, W. Wang, G. Zhao and L. Liu, *ACS Appl. Mater. Interfaces*, 2021, **13**, 54246–54257.

22. N. Sefidmooye Azar, J. Bullock, V. R. Shrestha, S. Balendhran, W. Yan, H. Kim, A. Javey and K. B. Crozier, *ACS Nano*, 2021, **15**, 6573–6581.

23. X. Liu, S. Hu, J. Luo, X. Li, J. Wu, D. Chi, K. W. Ang, W. Yu and Y. Cai, *Small*, 2021, **17**, 2100246.

24. X. Tai, Y. Chen, S. Wu, H. Jiao, Z. Cui, D. Zhao, X. Huang, Q. Zhao, X. Wang, T. Lin, H. Shen, X. Meng, J. Wang and J. Chu, *RSC Adv.*, 2022, **12**, 4939–4945.

25. P. Feng, S. Zhao, C. Dang, S. He, M. Li, L. Zhao and L. Gao, *Nanotechnology*, 2022, **33**, 255204.

26. X. Zhu, L. Chen, X. Tang, H. Wang, Y. Xiao, W. Gao and H. Yin, *Appl. Phys. Lett.*, 2022, **120**, 091109.

27. J. Lu, Z. Deng, Q. Ye, Z. Zheng, J. Yao and G. Yang, *Small Methods*, 2022, **6**,

2101046.

28. J. Quereda, S. Kuriakose, C. Munuera, F. J. Mompean, A. M. Al-Enizi, A. Nafady, E. Diez, R. Frisenda and A. Castellanos-Gomez, *npj Flex. Electron.*, 2022, **6**, 23.
29. J. Ma, Q. Gu, Y. Liu, J. Lai, P. Yu, X. Zhuo, Z. Liu, J. H. Chen, J. Feng and D. Sun, *Nat. Mater.*, 2019, **18**, 476–481.
30. Y. Lu, J. Chen, T. Chen, Y. Shu, R. J. Chang, Y. Sheng, V. Shautsova, N. Mkhize, P. Holdway, H. Bhaskaran and J. H. Warner, *Adv. Mater.*, 2020, **32**, 1906958.
31. R. R. Ma, D. D. Xu, Z. Guan, X. Deng, F. Yue, R. Huang, Y. Chen, N. Zhong, P. H. Xiang and C. G. Duan, *Appl. Phys. Lett.*, 2020, **117**, 131102.
32. J. Chen, L. Li, P. Gong, H. Zhang, S. Yin, M. Li, L. Wu, W. Gao, M. Long, L. Shan, F. Yan and G. Li, *ACS Nano*, 2022, **16**, 7745–7754.
33. J. Chen, C. Tan, G. Li, L. Chen, H. Zhang, S. Yin, M. Li, L. Li and G. Li, *Small*, 2021, **17**, 2006496.
34. D. Kim, K. Park, J. H. Lee, I. S. Kwon, I. H. Kwak and J. Park, *Small*, 2021, **17**, 2006310.
35. S. Zhao, P. Luo, S. Yang, X. Zhou, Z. Wang, C. Li, S. Wang, T. Zhai and X. Tao, *Adv. Opt. Mater.*, 2021, **9**, 2100198.
36. Z. Sun, P. Yu, F. Wang, F. Wang, Y. Yao, X. Zhan, Z. Wang and J. He, *Appl. Phys. Lett.*, 2022, **120**, 103506.
37. Y. Zhang, J. Chen, C. Chen, T. Xu, H. Gao, Z. Dong, Y. Zhang, C. Li, Q. Yu, W. Yu, J. Miao, P. Wang, W. Ren, A. Pan and K. Zhang, *Appl. Phys. Lett.*, 2022, **120**, 131104.
38. R. Maiti, C. Patil, M. A. S. R. Saadi, T. Xie, J. G. Azadani, B. Uluutku, R. Amin, A.

F. Briggs, M. Miscuglio, D. Van Thourhout, S. D. Solares, T. Low, R. Agarwal, S. R. Bank and V. J. Sorger, *Nat. Photonics*, 2020, **14**, 578–584.

39. F. Sun, C. Nie, J. Fu, W. Xiong, Y. Zhi and X. Wei, *ACS Appl. Mater. Interfaces*, 2022, 10.1021/acsami.1022c05038.
40. H. Shang, H. Chen, M. Dai, Y. Hu, F. Gao, H. Yang, B. Xu, S. Zhang, B. Tan, X. Zhang and P. A. Hu, *Nanoscale Horiz.*, 2020, **5**, 564–572.
41. V. Selamneni, S. K. Ganeshan and P. Sahatiya, *J. Mater. Chem. C*, 2020, **8**, 11593–11602.
42. M. Long, F. Liu, F. Ding, Y. Wang, J. Ye, R. Xie, H. Wang, M. Xu, F. Wang, Y. Tu, T. Han, F. Li, Z. Zhang and L. Liu, *Appl. Phys. Lett.*, 2020, **117**, 231104.
43. J. Yao, F. Chen, J. Li, J. Du, D. Wu, Y. Tian, C. Zhang, J. Yang, X. Li and P. Lin, *J. Mater. Chem. C*, 2021, **9**, 13123–13131.
44. C. Tan, S. Yin, J. Chen, Y. Lu, W. Wei, H. Du, K. Liu, F. Wang, T. Zhai and L. Li, *ACS Nano*, 2021, **15**, 8328–8337.
45. J. J. Tao, J. Jiang, S. N. Zhao, Y. Zhang, X. X. Li, X. Fang, P. Wang, W. Hu, Y. H. Lee, H. L. Lu and D. W. Zhang, *ACS Nano*, 2021, **15**, 3241–3250.
46. Y. Lu, T. Chen, N. Mkhize, R. J. Chang, Y. Sheng, P. Holdway, H. Bhaskaran and J. H. Warner, *ACS Nano*, 2021, **15**, 19570–19580.
47. M. Yamamoto, K. Ueno and K. Tsukagoshi, *Appl. Phys. Lett.*, 2018, **112**, 181902.
48. T. H. Tsai, Z. Y. Liang, Y. C. Lin, C. C. Wang, K. I. Lin, K. Suenaga and P. W. Chiu, *ACS Nano*, 2020, **14**, 4559–4566.
49. N. Flöry, P. Ma, Y. Salamin, A. Emboras, T. Taniguchi, K. Watanabe, J. Leuthold and L. Novotny, *Nat. Nanotechnol.*, 2020, **15**, 118–124.

50. J. He, H. Chen, Q. Zhao, Y. Wang, Y. Pan, S. Huang, F. C. C. Ling, S. Wang and S. Su, *J. Mater. Chem. C*, 2021, **9**, 9484–9491.

51. D. K. Kim, S. B. Hong, J. Kim and M. H. Cho, *J. Mater. Chem. C*, 2021, **9**, 15150–15157.

52. J. M. Choi, H. Y. Jang, A. R. Kim, J. D. Kwon, B. Cho, M. H. Park and Y. Kim, *Nanoscale*, 2021, **13**, 672–680.

53. M. T. Hossain, M. Das, J. Ghosh, S. Ghosh and P. K. Giri, *Nanoscale*, 2021, **13**, 14945–14959.

54. W. Wang, Y. Meng, W. Wang, Z. Zhang, P. Xie, Z. Lai, X. Bu, Y. Li, C. Liu, Z. Yang, S. Yip and J. C. Ho, *Adv. Funct. Mater.*, 2022, 10.1002/adfm.202203003.

55. M. Du, X. Cui, H. H. Yoon, S. Das, M. D. G. Uddin, L. Du, D. Li and Z. Sun, *ACS Nano*, 2022, **16**, 568–576.

56. F. Fang, Y. Wan, H. Li, S. Fang, F. Huang, B. Zhou, K. Jiang, V. Tung, L. J. Li and Y. Shi, *ACS Nano*, 2022, **16**, 3985–3993.